Hindawi
Advances in Materials Science and Engineering
Volume 2018, Article ID 8563054, 11 pages
https://doi.org/10.1155/2018/8563054

Research Article

Repairing 2024 Aluminum Alloy via Electrospark Deposition Process: A Feasibility Study

G. Renna,[1] P. Leo,[1] G. Casalino,[2] and E. Cerri[3]

[1]*Innovation Engineering Department, University of Salento, Via per Arnesano s,n, 73100 Lecce, Italy*
[2]*DMMM, Politecnico di Bari, Viale Japigia 182, 70126 Bari, Italy*
[3]*Department of Engineering and Architecture, University of Parma, v.le G. Usberti 181/A, 43124 Parma, Italy*

Correspondence should be addressed to P. Leo; paola.leo@unisalento.it

Received 4 November 2017; Accepted 26 February 2018; Published 27 March 2018

Academic Editor: Antonio Riveiro

Copyright © 2018 G. Renna et al. This is an open access article distributed under the Creative Commons Attribution License, which permits unrestricted use, distribution, and reproduction in any medium, provided the original work is properly cited.

The electrospark deposition (ESD) technique has been studied as a potential method to repair locally damaged 2024 rolled sheets supplied in natural-aged (T4) and artificial-aged (T6) conditions. The 2024-T4 and 2024-T6 tensile samples were first notched, and then the notches were filled (repaired) by ESD with the same aluminum alloy. The effect of process parameters on the microstructure of the filling material and the substrate properties was studied by optical and scanning electron microscopy. Tensile and hardness tests were performed. The tensile test showed that T4 and T6 as-repaired specimens had low tensile properties, which was due to defectiveness and residual stress caused by high cooling rate during reparation. However, the as-repaired specimens were heat-treated at either 135°C or 190°C to improve the mechanical properties. A better yield strength was observed for the T4 heat-treated alloy. The ductility and ultimate tensile strength did not change, being mainly affected by voids and microcracks.

1. Introduction

The need to reduce operating, maintenance, and waste-related costs of an aircraft has prompted aeronautical industries to develop new repair procedures for aeronautical components. Besides, because of the extreme cost of materials and labor for fabricating high-value component, it is also necessary to repair all those components which are affected milling ball indentation and cutter pull out, which occur during the manufacturing process [1, 2]. New repairing technologies should overcome the limitations of the actual ones and be able to operate in the maintenance facility, which would avoid transporting it in a repairing workshop or sending the worn-out part to the original manufacturer [3].

Aluminum alloy 2024 was a forerunner of a variety of 2xxx series alloy that is widely applied in the aerospace industry for its superior properties such as high strength-to-weight ratio, very good resistance to fatigue crack growth, and good fracture toughness [4, 5]. It is commonly supplied in the T4 or T6 temper since such treatments give good mechanical properties. Generally, the 2024 parts used in aviation for damage tolerance applications, such as the lower wing skins and fuselage structure of commercial aircraft, usually easily undergo localized corrosion (i.e., pitting and exfoliation) especially in chloride-containing environment [6, 7].

Unfortunately, the conventional fusion welding methods (i.e., tungsten inert gas welding (TIG), plasma transferred arc and electron beam welding, and laser cladding) are not suitable for repairing this alloy [1, 5]. It has been proved that several problems like solidification cracking, grain boundary melting in the base metal (liquation cracking), and changes in metallurgical structure would arise mainly due to the high thermal process input [8–14].

Electrospark deposition (ESD) technology is an effective method for the deposition of anticorrosion and wear-resistance coatings. It is a low heat input pulsed micro-bonding process that uses high-energy density and short duration of electrical pulses, typically ranging from a few

Table 1: Chemical composition (wt. %) for the alloy AA2024.

Composition	Ti	Zi	Fe	Cr	Si	Cu	Mn	Mg	Al
AA2024	<0.15	<0.25	<0.50	<0.5	<0.5	3.8–4.9	0.3–0.9	1.2–1.8	Bal.

microseconds to milliseconds, to deposit the electrode material onto the component's surface. It appears to be a very interesting and economic solution for the restoration and refurbishment of worn or damaged high-valued parts, especially those materials ordinarily considered poor-weldable by conventional repairing processes [2, 15–21].

In this technique, an electrical arc is pulsed between a rotating consumable electrode (anode) and the workpiece/substrate (cathode) to produce the deposit by detaching small droplets of material from the electrode and ejecting towards substrate. During the process, the electrical arc is pulsed with a frequency varying between 0.1 and 4 KHz using a high-frequency power supply [22, 23].

The short pulse duration and high-pulse frequency induce both very fast cooling rate and a rapid solidification process in combination with a small amount of material transferred during each pulse ESD technology. This rapid solidification rate, believed to approach 10^5-$10^{6°}$C/s, results in the refinement of the microstructure to either the nanostructured or amorphous level [23]. The solidification mode of the deposited alloy, as well as the resulting grain morphology, is controlled mainly by the thermal condition that exists at the beginning of the solidification. Otherwise, the fine scale microstructure is controlled primarily by the postsolidification cooling rate [17].

This innovative technology has gained much interest in the repairing field since it can offer a variety of advantages including low pollution, technical feasibility for metal deposition in atmospheric pressure, and welding equipment handling and transportability. Moreover, the reduction of residual stress and distortion compared to the other fusion processes renders this technique highly applicable to those materials possessing a high tendency to crack during welding, such as superalloys, MCrAlY, and thermally sensitive materials (2000 series aluminum alloy) [22–24].

Many works have studied the mass transfer that occurs during the ESD process [25–27], which is paramount to produce a high wear-resistant coating [28–32]. The relationship between process parameters and the deposit structure has been also investigated [33–36]. Only few studies are related to the utilisation of ESD as a repair technology. Farhat [24] determined that the repair of a locally damaged NiCoCrAlY or CoNiCrAlY coating can be done by ESD to further extend the lifetime of coatings. While Johnson showed the possibility of repairing a single crystal turbine blade with low net heat input free from distortion [37].

Besides, to date investigations focused on assessment of ESD as repair technology, not concerning thermally sensitive materials such as the 2024 alloy.

In this paper, a comparative study between deposits prepared by ESD on AA2024 standard dog-bone substrates both in natural-aged (T4) and artificial-aged (T6) states has been presented. Detailed analyses of the microstructure modification of the filling alloy and the effect of process parameters on the substrate properties and microstructure were performed.

Furthermore, the as-repaired specimens were heat treated at 135°C and 190°C to reduce the detrimental effect of residual stresses on the mechanical properties. Hence, also the effect of postrepair heat treatment (PRHT) on the microstructure and mechanical properties of the repaired specimens was investigated.

2. Experimental Methods

AA2024 aluminum alloy was used for the electrode and the substrate materials. ESD substrate was supplied as T4 and T6 rolled plates. Chemical components (wt. %) of the AA2024 alloy are listed in Table 1.

Dog-bone specimens were realized from 4 mm thick plates (Figure 1(a)). A notch was machined in the midsize of the dog-bone specimens to be later filled up with the electrode material, as shown in Figure 1(b). Deposition was carried out using a hand-held gun at room temperature with argon (Ar) protection, which avoids contamination of the deposit zone by interstitial elements such as oxygen or nitrogen. During deposition, the electrode rotated at 1200 rpm speed. The electrospark deposition process parameters are shown in Table 2, where E is the value of the electric arc pulse energy in Joule. These parameters are based on a previous study of Leo et al. [36].

The substrate was kept in a fixed position, while the hand-held gun was moving according to three orthogonal XYZ axes. At the beginning, the semicircular shape of the notch was coated by adjacent depositions. The depositions had circular shape to fit the semicircular shape of the notch. The close semicircular depositions were realized to cover the entire surface of the notch along the y-axis. The filling was obtained by superimposing several depositions along the Z direction (Figure 1(b)). Then, the samples were postrepair heat treated (PRHT) for 2 h at 135°C and for 6 h at 190°C. All samples were air-cooled. Holding times and temperatures are displayed in Table 3. Samples were sectioned across the deposit center, embedded in epoxy resin and then polished to a mirror finish. Analyses were performed on the XZ section in the as-polished condition to assess the metallurgical health within the deposit and in the bonding zone. The microstructure was revealed by etching with Keller's reagent. Three complementary methods were used to study the microstructure: stereo microscopy (SM), optical microscopy (OM), and scanning electron microscopy (SEM) with EDS. The grain structure of substrate was revealed by electropolishing (20% perchloric acid and 80% ethanol at 0°C; electropolishing parameter: 15 V and 60 s), anodic

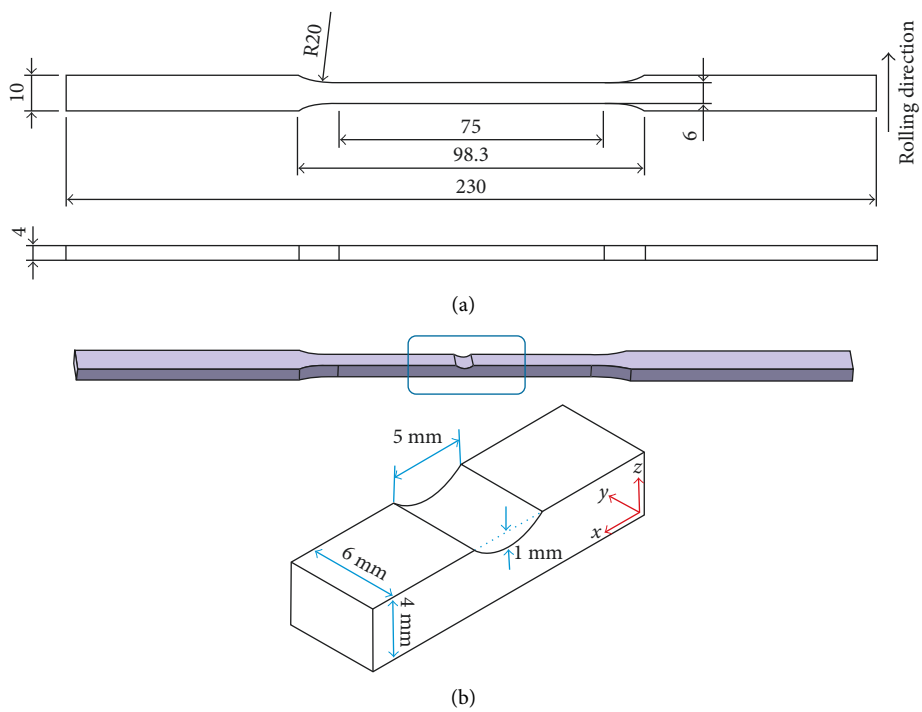

Figure 1: (a) Sizes of the dog-bone specimen for tensile tests and (b) draft of defect dimensions machined into dog-bone specimens. These defects will be machined into one-half of the specimens and subsequently filled with ESD.

Table 2: Process parameters used in the experiments.

E (J)	Ar (l/min)	Electrode rotation speed (rpm)
0.9	20	1200

Table 3: PRHT on dog-bone specimens of AA2024 in both T4 and T6 conditions.

	Temperature (°C)	Holding time (h)	Cooling
T_{135_2}	135	2	Air cooling
T_{190_6}	190	6	Air cooling

oxidation (Barker etching; anodizing parameters: 20 V and 80 s), and subsequent investigation under polarized light in OM.

The defect areas inside the deposit and the length of cracks at the substrate/deposit interface on the XZ plane (Figure 1(b)) were obtained using the NIS software for imaging analysis. NIS-Elements is a NIKON software supplied with Epiphot 200 OM. Defects area percentage was measured as the sum of the defect areas divided by the area of the repaired zone. Moreover, using ImageJ software, both Feret's diameter and the shape factor (f_{circle}) of the filling defects have been evaluated. The shape factor comes from the following equation:

$$f_{\text{circle}} = \frac{4\pi A}{P^2}, \quad (1)$$

where P is the perimeter and A is the area of defect. For a perfect spherical defect, the shape factor is one, while for a strongly elongated defect, it is very close to zero. Particularly, two main morphological classes of defects were considered in this study:

(i) Defects with $0 < f_{\text{circle}} \leq 0.5$

(ii) Defects with $0.5 < f_{\text{circle}} \leq 1$

Microhardness tests were performed with the load of 100 g for 15 s. Microhardness measurements were carried out on the XZ plane following a grid arrangement parallel to the top surface of the deposit in accordance with ISO 6507-1: 2005. The distance between the indentations both in the horizontal and vertical direction was 100 μm. Then, the average values of microhardness were calculated considering all the indentation made in the deposit zone and in the BM, respectively. These measures were carried out on both as-repaired and PRHT samples. Tensile tests were carried out, at room temperature, in a universal testing machine in accordance with ISO 6892-1:2009 perpendicularly to the rolling direction (RD). The displacement control, at an initial strain rate of 0.25 mm/min, was used. Strains were measured with an axial extensometer with a gauge length of 12.5 mm.

3. Results and Discussion

3.1. Base Material Characterization. In AA2024-T4 alloy, the hardening mechanism is due to the Guinier–Preston zone (G–P zone) in the grains that hinder dislocation movement. While the AA2024-T6 reaches the peak hardness due to a finer transitional precipitates distribution that remains coherent with the solid-solution matrix, it contributes to precipitation strengthening. Both G–P zone (~10 nm thick

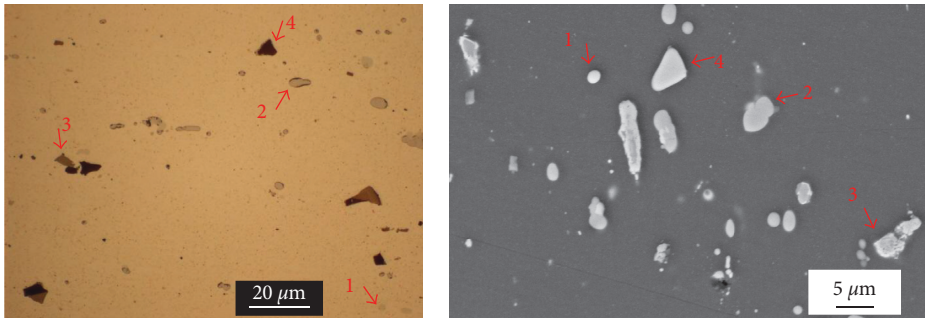

(a) (b)

Figure 2: (a) OM and (b) SEM image of AA2024 BM after chemical etchant: (1) mainly roughly spherical particles Al_2CuMg, (2) light grey particles $CuAl_2$, (3) light brown particles $(Mn, Fe)_3SiAl_{12}$, and (4) dark brown phase Al(Cu, Fe, Mn).

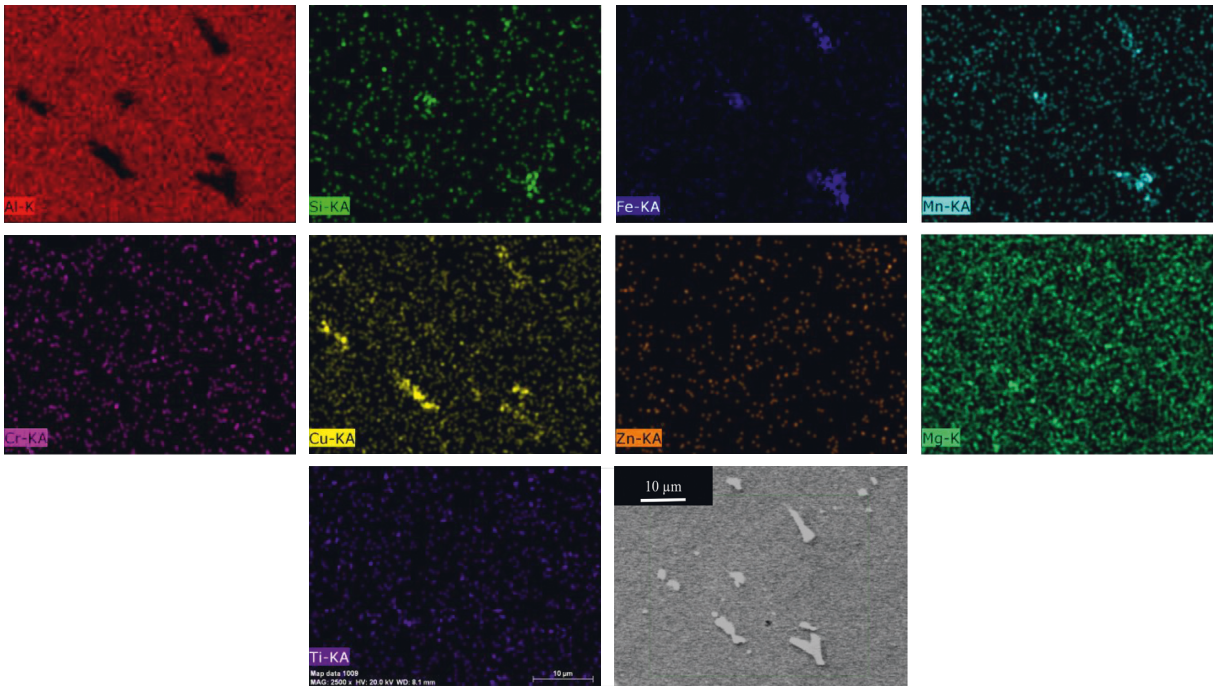

Figure 3: Elemental map of 2024 BM. The analysis confirms the chemical composition of typical intermetallic particles.

and 100 nm in diameter) and the precipitate particles (larger than G–P zone) are too small to be clearly resolved by OM or SEM microscopy [4, 5, 38]. Figure 2(a) presents the microstructure of the AA2024 alloy base material (BM) in the perpendicular direction to rolling manufacturing. OM and SEM micrographs of 2024, in T4 (Figure 2(a)) and T6 (Figure 2(b)) states, respectively, show the aluminum matrix together with a series of intermetallic particles of different morphologies and sizes. According to the literature and the SEM/EDS analysis, the main spherical intermetallic particles are Al_2CuMg (S-phase) (1, Figures 2(a) and 2(b)), while the light grey particles are Al_2Cu (θ phase) (2, in Figures 2(a) and 2(b)). Moreover, $(Mn, Fe)_3SiAl_{12}$ (light brown, 3, Figures 2(a) and 2(b)) and Al(Cu, Fe, Mn) phases (dark brown, 4, Figures 2(a) and 2(b)) were detected. They were as large as 10 μm and had an irregular shape. Furthermore, according to the literature, the fine dispersoids in the Al matrix can be either $Cu_2Mn_3Al_{20}$ or Al_2Cu [5, 39]. The element mapping (Figure 3) of the BM confirmed the presence of those phases.

The mechanical properties of the base material both in the T4 and T6 conditions, at room temperature, are presented in Table 4 [5].

3.2. Defectiveness and Microstructure within the Fillings. Figures 4(a) and 4(b) show the SM pictures of the notch after filling with the ESD process. Figure 4(c) is an OM micrograph of a *XZ* plane of the electrospark filling. It can be clearly seen that the top surface was continuous and without visible cracks or other defects (Figures 4(a) and 4(b)). However, some defects are shown in Figure 4(c). The main defects detected in the analyzed fillings were voids with different morphologies and microcracks that extended both perpendicularly and parallel to the substrate/filling interface. In particular, the typical voids identified within the fillings had

Table 4: Mechanical properties of base material (BM) in T4 and T6 conditions.

Material	Yield strength (MPa)	Ultimate tensile strength (MPa)	Elongation (%)	Vickers hardness ($HV_{0.1/15}$)
AA2024-T4	339	485	29	141 ± 1.1
AA2024-T6	482	516	16,4	158 ± 2.6

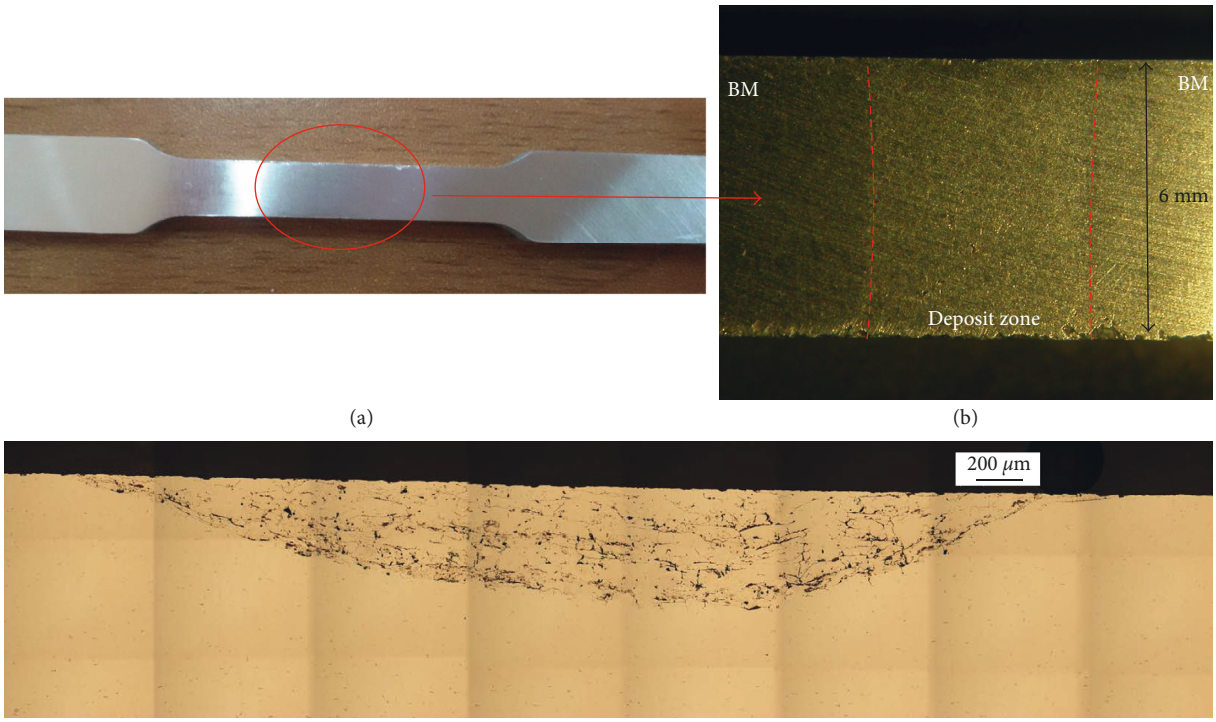

(a) (b)

(c)

Figure 4: (a, b) The repair from top view and (c) typical cross section micrograph of electrospark deposit.

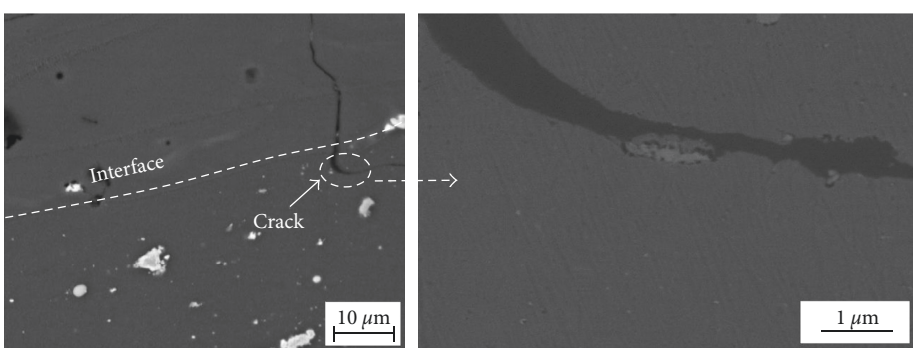

(a) (b)

Figure 5: (a) SEM micrographs showing cracking behavior in the deposit/base metal interface for the sample repaired and (b) SEM image suggesting the delineation of the crack paths by resolidified products, typical of liquation cracking.

three geometries, that is, small spherical voids (gas porosity), large, random-shaped voids (bridging porosity), and thin void layer (laminar porosity) [36]. The formation of these discontinuities depended strongly on the amount and localization of the fused material. During the manual deposition, the selected electrical parameters, the distance of the electrode to workpiece surface, and the force on the electrode did not remain constant during the deposition process [19, 36]. All the previous aspects changed the quantity of the metal that melted and/or evaporated. Therefore, peaks and valley formed on the surface, which appeared corrugated and showed voids [19, 30, 31]. Cracking within the filling is believed to be the result of the thermal stress, which builds up during cooling and solidification of

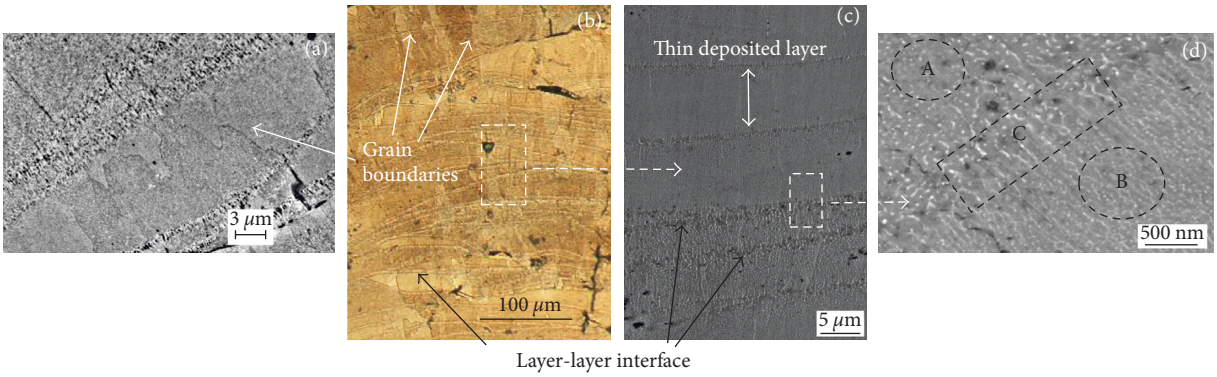

Figure 6: OM and SEM images of microstructure parallel to build direction: (b, c) layered deposit (morphology cross section), (a) fine microstructure to layer-layer interface and within of the layers, and (d) long, slender columnar-like grains.

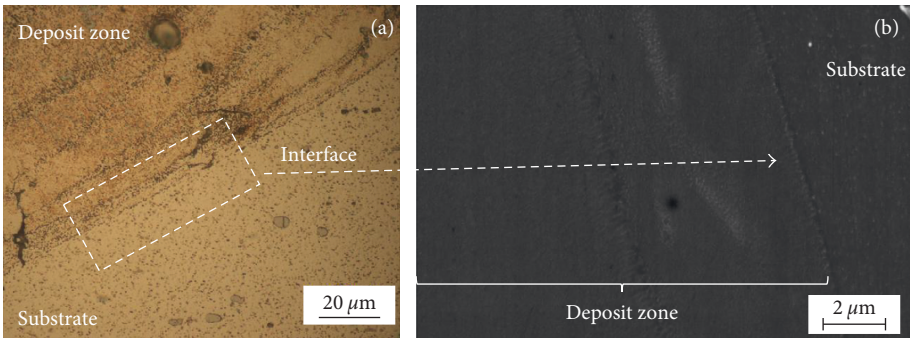

Figure 7: (a) OM and (b) SEM micrographs showing the deposit/base metal interface for the sample repaired.

the deposited material. The residual thermal stress in the filling was always tensile [40, 41]. Moreover, from the analysis of the substrate/filling interface, it was observed also that both the substrates in T4 and T6 states were characterized by cracks that preferentially extended along the grain boundaries (Figure 5(a)). High magnification SEM image outlined the crack path by the resolidified products, which are typical of the liquation cracking phenomenon (Figure 5(b)). Simultaneously, the rapid cooling from the ESD process induced a great thermal strain that opened the liquated zones. In fact, 2024 aluminum alloy is susceptible to solidification and liquation cracking having large range of solidification, high thermal expansion, large shrinkage, and many alloying elements [10, 41].

Optical and scanning electron micrographs on the *XZ* plane of the filling are shown in Figure 6. Numerous superimposed linear tracks can be observed clearly (Figures 6(b) and 6(c)) due to the remelting which was caused by the superimposed layer (layer-layer interface). Moreover, these layers differed in size and overlapped one over the other. The random size layers just revealed the instability in the manual deposition process. The average thickness of the several deposited layers was calculated through the application of intercept method. It was then determined to be $\sim 12.4 \pm 6.1\,\mu$m. In addition, columnar grain structure grew perpendicularly to the substrate (Figures 6(a) and 6(b)). These columnar grains grew epitaxially along the crystallographic direction of previously solidified grain, through multiple layers, producing microstructure normal to the deposition layers [10, 36, 38, 42]. The coating microstructure was fine due to the high cooling rate [15, 16]. Moreover, some layers were characterized by a cellular dendritic microstructure (highlighted by the circle B in Figure 6(d)), and some other layers showed a uniform distribution of fine small second phase particles (appearing as light point in the circle A of Figure 6(d)). Moreover, the interlayer thin zone exhibited a coarse microstructure, generally equiaxed (highlighted by the box C in Figure 6(d)). These different microstructure morphologies in thin deposit layers can be attributed to the variable solidification conditions in the volume of the molten splat (liquid phase) [16, 43]. The interface between the filling and substrate is shown in Figure 7. The filling formed a metallurgical bound with the substrate (Figure 7).

3.3. Analysis of Defects. The defects in the filling material and at the filling/substrate interface were examined in detail. In the filling, for all the samples obtained, some randomly distributed defects with spherical and laminar shapes were observed in the deposit volume. The average area fraction of these defects was 2.5%, which can be considered acceptable. Figures 8(a) and 8(b) display the plots of the Feret diameter as a function of the shape factor (f_{circle}) and the percent distribution of the defects having shape factor (f_{circle}) between 0 and 0.5 and 0.5 and 1, respectively. As exhibited in Figure 8(a), the defects of larger size were the most irregular ones and the fillings were mainly characterized by laminar defects (shape factor included between 0 and 0.5). In fact, the

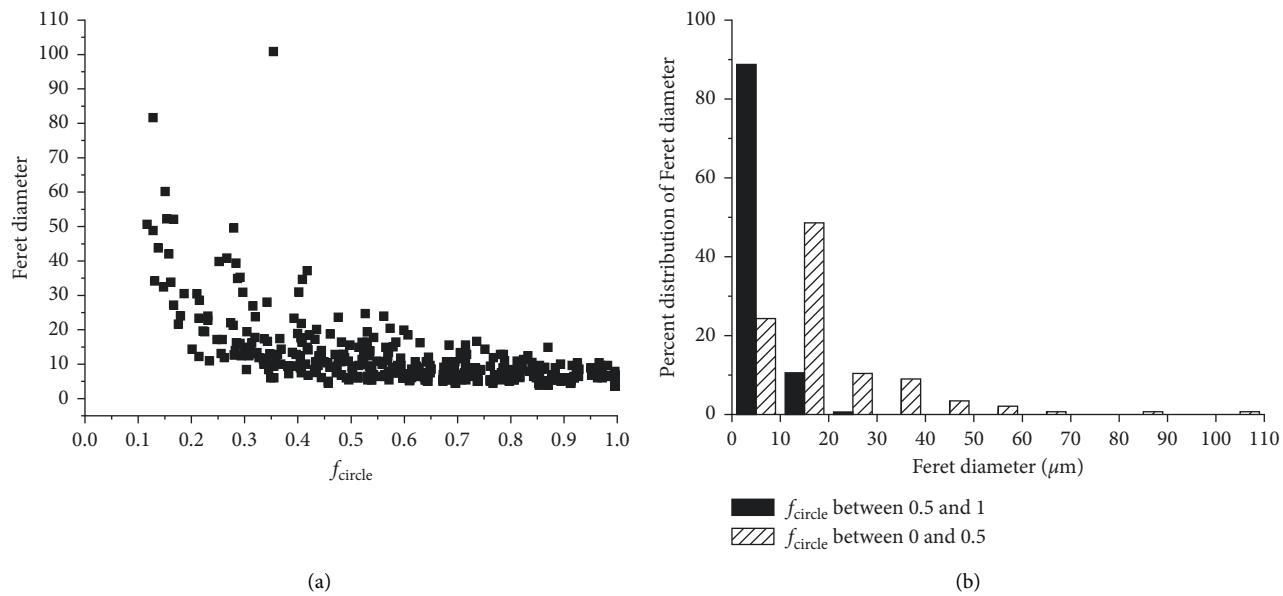

Figure 8: Analysis of defects within the volume of the deposit obtained with the electrical parameters is reported in Table 2. (a) Feret diameter versus f_{circle} of defects and (b) Feret diameter distribution of the defects having shape factor (f_{circle}) between 0 and 0.5 and 0.5 and 1.

Feret diameter distribution of the defects shown in Figure 8(b) illustrated how the almost totality of defects with f_{circle} between 0 and 0.5 had length shorter than 20 μm. In addition, 50% of them had diameters between 10 μm and 20 μm, but with defects of considerable extension. The tensile thermal stress increased during the growth of the filling, causing large cracks in the filling and delamination at the weak interface bond. The small size voids were created by the formation of asperities or trapped gas. Figure 8(b) shows that spherical defects (f_{circle} 0.5–1) were mostly distributed (90%) in the lower class of the Feret diameters (up to 10 μm) while the remaining had Feret diameters between 10 and 30 μm. Regarding the defects at the substrate/filling interface, for the two different treatment conditions of the BM (T4 and T6 states), the values of the average crack length and the ratio between the crack number (N°_{tot}) and interface length (mm) examined are obtained and reported in Table 5. In addition, Figure 9 shows the distribution of the length of cracks that propagated in the substrate from the substrate/filling interface in the BM state T4 and T6. It is noteworthy that the ESD process generated the same N°_{tot}/mm value regardless of the BM state (T4 or T6) and a considerable rise of the average crack length in the T6 BM. The increase in the average crack length observed in 2024-T6 sample was due to the high hardness of the substrate. Once triggered, the cracks propagated more easily thanks to the brittleness of the region. In fact, observing the crack length distribution plots, the deposition on the 2024-T6 sample produced lower crack percentage for length fields below 15 μm and a rise in the percentage of longer cracks with consequent rise in the crack length field variation. Therefore, the depositions made on the 2024-T6 induced greater defects at the interface than the depositions made on the 2024-T4.

Table 5: Average crack length and ratio between the cracks number and interface length examined both in the case in which the filling was performed on the base material in T4 and T6 states.

	Average crack length (μm)	N°_{tot} (mm)
2024-T4	11.3 ± 7.2	10.7
2024-T6	26.5 ± 16	11.14

3.4. Mechanical Characterization

3.4.1. Microhardness. Figure 10 shows the microhardness profiles of the fillings and AA2024 substrate both in T4 and T6 conditions. The graph shows the average microhardness values detected at increasing distances from the substrate/deposit interface. Table 6 shows the average microhardness. In addition, the average microhardness values of the substrate measured at 100 μm from the coating interface are indicated. The hardness of the filling was generally lower than that of the substrate in all the samples examined (Figure 10 and Table 6). The decrease of the hardness was due to the aging in the base material and to some defects, which formed inside the coating. Moreover (Figure 10), in the repaired zone, the average microhardness values remained almost constant, which confirm that there were no significant microstructural changes along the thickness of the repaired zone. The results in Table 6 suggest that the microhardness of the substrate close to the interface did not vary compared to that of the BM zone. Therefore, the mechanical properties of the substrate were not altered. Furthermore, the results showed that the postrepair heat treatment (PRHT) performed on samples had no effect on the hardness of the filling. In fact, it remained almost constant regardless of the heat treatment temperature employed.

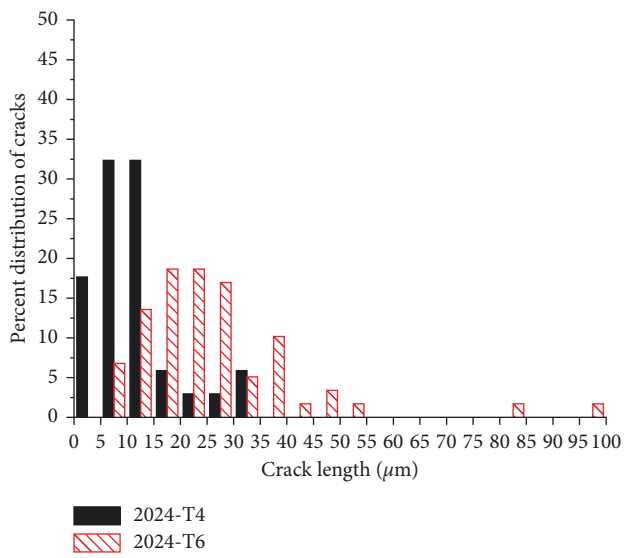

Figure 9: Analysis of defects to substrate/filling interface: distribution of the crack length that propagates in the substrate from the interface both in the case in which the filling was performed on the base material in T4 and T6 states.

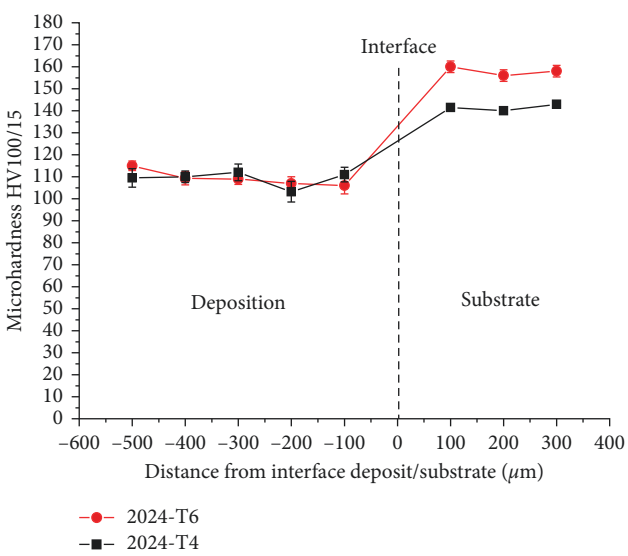

Figure 10: Microhardness measurement through the filling layer and AA2024 substrate both in T4 and T6 conditions.

The hardness of 2024-T4 substrate, that was underaged, increased after the T_{190_6} PRHT due to the precipitation of more hardening particle [38]. Due to overaging, the hardness value of the 2024-T6 substrate, that was peak aged, decreased with the increasing time and temperature of the heat treatment. In fact, it is known that if precipitate particles are large and widely spaced, they can be readily bypassed by moving dislocations which bow out between them and rejoin by a mechanism first proposed by Orowan [4].

Table 6: Average hardness value ($HV_{100/15}$) with the locations each sample.

Sample	Filling	Substrate	Interface
2024-T4 repaired	109.5 ± 5	141 ± 1.1	140 ± 1.1
2024-T4 repaired + T_{135_2}	107 ± 5	141 ± 2.8	140 ± 2.8
2024-T4 repaired + T_{190_6}	104 ± 4	148 ± 1.8	149 ± 1.8
2024-T6 repaired	109.5 ± 5	158 ± 2.6	157 ± 2.6
2024-T6 repaired + T_{135_2}	107.7 ± 5	156 ± 3.4	156 ± 3.4
2024-T6 repaired + T_{190_6}	107.3 ± 6.9	151 ± 1.2	150 ± 1.2

3.4.2. Tensile Behavior. The tensile test was carried out to determine the behavior of the repaired specimens. Table 7 contains the values of the yield stress (σ_y), ultimate tensile strength (UTS), the load at fracture, strain at fracture (elongation e_f), and cross-sectional area (S_0) for as-received BM in T4 and T6 states, as-received BM notched, and repaired specimens both in untreated and treated T_{135_2} and T_{190_6} states. The stress-strain curves obtained are shown in Figure 11. From the results of the tensile tests, both as-repaired and PRHT samples displayed a decay of the mechanical properties compared BM (both notched and unnotched 2024 samples). This was probably caused by the presence of widespread defects inside the deposit and at the substrate/deposit interface as well as by different microstructural characteristics of the deposit and the BM. The yield stress (σ_y) and the ultimate tensile strength (UTS) of the as-repaired samples and PRHT samples were lower with respect to the notched samples. At the same time, a reduction in ductility owing to the defects present within the deposit and at the interface was observed. Porosity in the deposit led to stress concentration, so the crack easily started and propagated throughout the sample thickness. Moreover, the cracks at the interface induced the low tensile strength rupture. An increase of the mechanical properties (Table 7) was obtained by the high temperature and long duration PRHT treatment. The yield strength and UTS of the PRHT samples were greater with respect to the as-repaired samples. The T_{135_2} heat treatment increased the tensile strength of the 2024-T4 samples of 17 MPa and the yield strength of 34 MPa, while the T_{135_2} heat treatment increased the tensile strength of the 2024-T6 samples of 16 MPa and the yield strength of 39 MPa. Likewise, the T_{190_6} heat treatment increased the tensile strength of the 2024-T4 samples of 16 MPa and the yield strength of 72 MPa, while the T_{190_6} heat treatment increased the tensile strength of the 2024-T6 samples of 18 MPa and the yield strength of 46 MPa. The improvements of σ_y and UTS were primarily due to the reduction of the residual stresses and/or to the increasing of hardness due to heat treatment. The role of the residual stress reduction was particularly effective in the case of the PRHT performed at 190°C on the 2024-T6 sample in which the rise in the yield strength was associated with the overaging of precipitated particles (Table 6), which leads to softening of microstructure. So, the PRHT at 190°C was more effective when carried out on the 2024-T4 sample since, in addition to a residual stress reduction, the heat treatment also led to an increase of the substrate hardness.

Table 7: Tensile test for the as-received BM in T4 and T6 states, as-received BM notched, the untreated repaired samples, and heat-treated T_{135_2} and T_{190_6} repaired samples.

Sample	σ_y (MPa)	F_y (N)	UTS (MPa)	Maximum load (N)	e_f (%)	S_0 (mm^2)
2024-T4	339	8315.7	485	11,893	29	24.53
2024-T4 notched	346	7480.52	503	10,877	13.3	21.62
2024-T4 notched T_{135_2}	213.3	4645.7	487.2	10610.9	12	21.78
2024-T4 repaired	257	6198.84	402	9696.24	9	24.12
2024-T4 repaired + T_{135_2}	291	7245.9	419	10,440	10.1	24.9
2024-T4 repaired + T_{190_6}	329.2	7966.64	442.5	10,202.2	5.51	24.2
2024-T6	482	11,852.4	516	12,691	16.4	24.59
2024-T6 notched	482	10,488.3	532	11,585	4.5	21.76
2024-T6 repaired	372	8965.2	439	10,579.9	4	24.1
2024-T6 repaired + T_{135_2}	411	9913.32	455	10,973	4.2	24.12
2024-T6 repaired + T_{190_6}	418.8	10,302.5	457.29	11,238.6	3.24	24.6

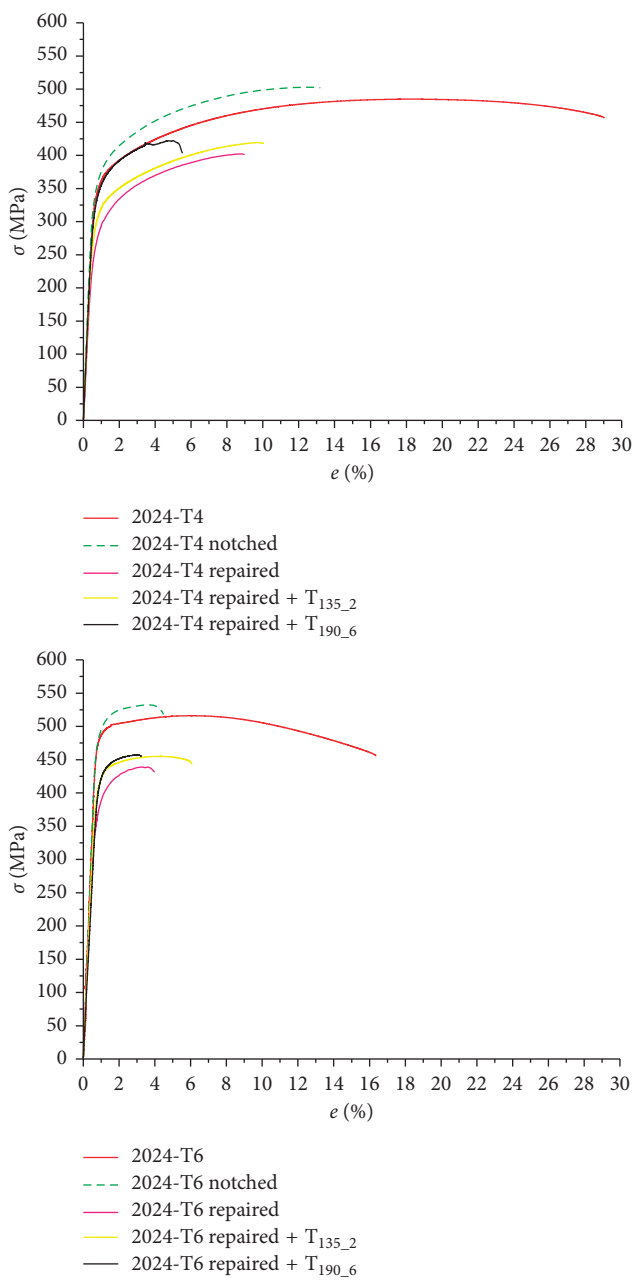

Figure 11: Tensile stress-strain curves.

4. Conclusion

The study of the 2024 aluminum alloy electrospark deposition process on a similar substrate brought the following evidences:

(1) The filling microstructure was layer by layer, very fine, and mixed with both cellular and equiaxed dendrites. In the filling layers, grains formed long columnar grains with a preferential growth along the build-up direction. The microstructure was strongly inhomogeneous due to the different cooling rates during the deposition process. The hardness of the deposited metal was lower than that of the substrate. The substrate did not present a heat affected zone.

(2) The reparation showed the presence of some defectiveness. Those defects, randomly distributed in the microstructure had spherical, casual, and laminar shapes. The average area fraction of these defects was 2.5% which is considered acceptable. It was estimated that the fillings had 63% of laminar and 37% spherical shape defects. The formation of defects with laminar morphology was mainly attributed to the tensile residual stresses. The length size of the cracks to interface was higher for the artificial aged deposition.

(3) The tensile properties of the repaired samples were lower compared to the notched ones (for both T6 and T4 states) due to the residual stress and defectiveness. The PRHT improved the yield strength of the repaired specimen by reducing residual stress. However, the ductility of the 2024 alloy was strongly reduced by the reparation process. PRHT at 190°C was most effective when carried out on 2024-T4 since, in addition to a residual stress reduction, the heat treatment also led to a rise in the substrate hardness.

Conflicts of Interest

The authors declare that they have no conflicts of interest.

References

[1] M. Brandt, *Laser Additive Manufacturing: Materials, Design, Technologies, and Applications*, Woodhead Publishing, Cambridge, UK, 2016.

[2] H. Paydas, A. Mertens, R. Carrus, J. Lecomte-Beckers, and J. Tchoufang Tchuindjang, "Laser cladding as repair technology for Ti–6Al–4V alloy: influence of building strategy on microstructure and hardness," *Materials and Design*, vol. 85, pp. 497–510, 2015.

[3] N. Price, *AESF/EPA Conference for Environmental and Process Excellence*, Environmental Protection Agency, Lake Buena Vista, FL, USA, 2004.

[4] I. J. Polmear, *Light Alloys: Metallurgy of the Light Metals*, Butterworth Heinemann, Oxford, UK, 1995.

[5] J. R. Davis, *ASM Specialty Handbook: Aluminum and Aluminum Alloy*, ASM International, Russell Township, OH, USA, 1993.

[6] F. C. Campbell, *Manufacturing Technology for Aerospace Structural Materials*, Elsevier, Amsterdam, Netherlands, 2006.

[7] C. M. Abreu, M. J. Cristòbal, P. Freitas et al., "Microstructure of the passive layer formed on AA2024-T3 aluminum alloy surface implanted with nitrogen," *Surface and Interface Analysis*, vol. 40, no. 3-4, pp. 290–293, 2008.

[8] R. Onjukka, "Welding vs riveting–which has the fatigue life for airplanes," *Welding International*, vol. 75, pp. 29–33, 1996.

[9] S. Kou, "Welding Metallurgy and Weldability of High Strength Aluminum Alloys," *Welding Research Council Bulletin*, vol. 320, pp. 1–20, 1986.

[10] M. F. Ghaini, M. Sheikhi, M. J. Torkamany, and J. Sabbaghzadeh, "The relation between liquation and solidification cracks in pulsed laser welding of 2024 aluminium alloy," *Materials Science and Engineering: A*, vol. 519, pp. 167–171, 2009.

[11] A. F. Norman, V. Drazhner, and P. B. Prangnell, "Effect of welding parameters on the solidification microstructure of autogenous TIG welds in an Al–Cu–Mg–Mn alloy," *Materials Science and Engineering: A*, vol. 259, pp. 53–64, 1999.

[12] W. R. Oates, *Materials and Applications*, vol. 3, AWS, Miami, FL, USA, 8th edition, 1972.

[13] H. Zhao, D. R. White, and T. DebRoy, "Current issues and problems in laser welding of automotive aluminium alloys," *International Materials Reviews*, vol. 44, pp. 238–266, 1999.

[14] X. Cao, W. Wallace, J. P. Immarigeon, and C. Poon, "Research and progress in laser welding of wrought aluminum alloys. II. Metallurgical microstructures, defects, and mechanical properties," *Materials and Manufacturing Processes*, vol. 18, no. 1, pp. 23–49, 2003.

[15] Y. J. Xie, M. C. Wang, and D. W. Huang, "Comparative study of microstructural characteristics of electrospark and Nd: YAG laser epitaxially growing coatings," *Applied Surface Science*, vol. 253, no. 14, pp. 6149–6156, 2007.

[16] Y. J. Xie and M. C. Wang, "Epitaxial MCrAlY coating on a Ni-base superalloy produced by electrospark deposition," *Surface and Coatings Technology*, vol. 201, no. 6, pp. 3564–3570, 2006.

[17] Y. J. Xie and M. C. Wang, "Microstructural morphology of electrospark deposition layer of a high gamma prime superalloy," *Surface and Coatings Technology*, vol. 201, no. 3-4, pp. 691–698, 2006.

[18] C. J. Chen, M. C. Wang, D. S. Wang, and Y. M. Liu, "Study on corrosion characteristic of high-energy micro-arc alloying of Al-Y electrode on AZ31 magnesium alloy," *Transactions of Materials and Heat Treatment*, vol. 28, pp. 106–110, 2007.

[19] S. Frangini and A. Masci, "A study on the effect of a dynamic contact force control for improving electrospark coating properties," *Surface and Coatings Technology*, vol. 204, no. 16-17, pp. 2613–2623, 2010.

[20] S. Frangini, A. Masci, and A. Di Bartolomeo, "Cr7C3-based cermet coating deposited on stainless steel by electrospark process: structural characteristics and corrosion behavior," *Surface and Coatings Technology*, vol. 149, no. 2-3, pp. 279–286, 2002.

[21] S. K. Tang, T. C. Nguyen, and Y. Zhou, "Materials transfer in electro-spark deposition of TiCp/Ni metal-matrix composite coating on Cu substrate," *Welding Research*, vol. 89, 2010.

[22] R. N. Johnson, "Robust coatings for corrosion and wear: the electrospark deposition process," in *Proceedings of the Tri-service conference on corrosion*, Battelle, Columbus, OH, USA, pp. 341–410, 1999.

[23] M. Brochu, D. W. Heard, J. Milligan, and S. Cadney, "Bulk nanostructure and amorphous metallic components using the electrospark welding process," *Assembly Automation*, vol. 30, no. 3, pp. 248–256, 2010.

[24] R. Farhat, *Repair of Damaged MCrAlY Coatings Targeting Petroleum Industry Applications*, McGill University, Montreal, QC, Canada, 2012.

[25] I. V. Galinov and R. B. Luban, "Mass transfer trends during electrospark alloying," *Surface and Coatings Technology*, vol. 79, no. 1–3, pp. 9–18, 1996.

[26] A. Lesnjajk and J. Tusek, "Processes and properties of deposits in electrospark deposition," *Science and Technology of Welding and Joining*, vol. 7, no. 6, pp. 391–396, 2002.

[27] C. Changjun, W. Maocai, L. Yiming, W. Dongsheng, and J. Ren, "Mass transfer trends and the formation of a single deposition spot during high-energy micro-arc alloying of AZ31Mg alloy," *Journal of Materials Processing Technology*, vol. 198, no. 1–3, pp. 275–280, 2008.

[28] W. F. Wang, M. C. Wang, F. J. Sun, Y. G. Zheng, and J.-M. Jiao, "Microstructure and cavitation erosion characteristics of Al-Si alloy coating prepared by electrospark deposition," *Surface & Coatings Technology*, vol. 202, no. 21, pp. 5116–5121, 2008.

[29] D. Liu, W. Gao, Z. Li, H. Zhang, and Z. Hu, "Electro-spark deposition of Fe-based amorphous alloy coatings," *Materials Letters*, vol. 61, no. 1, pp. 165–167, 2007.

[30] S. Cadney and M. Brochu, "Formation of amorphous Zr41.2Ti13.8Ni10Cu12.5Be22.5 coatings via the electrospark deposition process," *Intermetallics*, vol. 16, no. 4, pp. 518–523, 2008.

[31] S. Cadney, G. Goodall, G. Kim, A. Moran, and M. Brochu, "The transformation of an Al-based crystalline electrode material to an amorphous deposit via the electrospark welding process," *Journal of Alloys and Compounds*, vol. 476, no. 1-2, pp. 147–151, 2009.

[32] Y. J. Xie and M. C. Wang, "Isothermal oxidation behavior of electrospark deposited MCrAlX-type coatings on a Ni-based superalloy," *Journal of Alloys and Compounds*, vol. 480, no. 2, pp. 454–461, 2009.

[33] L. E. Brown, S. N. Hammond, and M. C. Nordin, "Method and apparatus for electrospark alloying," US Patent 6417477, 2002.

[34] A. Lešnjak and J. Tušek, "Processes and properties of deposits in electrospark deposition," *Science and Technology of Welding and Joining*, vol. 7, no. 6, p. 391, 2002.

[35] J. Liang, W. Gao, Z. Li, and Y. He, "Hot corrosion resistance of electrospark-deposited Al and Ni Cr coatings containing dispersed Y_2O_3 particles," *Materials Letters*, vol. 58, no. 26, p. 3280, 2004.

[36] P. Leo, G. Renna, and G. Casalino, "Study of the direct metal deposition of AA2024 by electrospark for coating and reparation scopes," *Applied Sciences*, vol. 7, no. 12, p. 945, 2017.
[37] R. N. Johnson, "Alternative coatings for wear and corrosion: the electrospark deposition process," in *Proceedings of the AESF Conference for Environmental Excellence*, Lake Buena Vista, FL, USA, January 2002.
[38] D. A. Porter and K. E. Easterling, *Phase Transformations in Metals and Alloys*, Chapman & Hall, London, UK, 1992.
[39] L. F. Mondolfo, *Aluminium Alloys: Structure and Properties*, Butterworth, Oxford, UK, 1976.
[40] Z. Chen and Y. Zhou, "Surface modification of resistance welding electrode by electro-spark deposited composite coatings: part I. Coating characterization," *Surface & Coatings Technology*, vol. 201, no. 3-4, pp. 1503–1510, 2006.
[41] W. Jian-sheng, M. Hui-min, Y. Hong-ying, F. Zi-shuan, and S. Dong-bai, "Characterization and wear behavior of WC-0.8Co coating on cast steel rolls by electro-spark deposition," *International Journal of Minerals, Metallurgy and Materials*, vol. 16, p. 707, 2009.
[42] R. W. Messler, *Principles of Welding*, John Wiley & Sons Inc., New York, NY, USA, 1999.
[43] W. Kurz and D. J. Fisher, *Fundamentals of Solidification*, Trans Tech Publications, Switzerland, 4th edition, 1998.

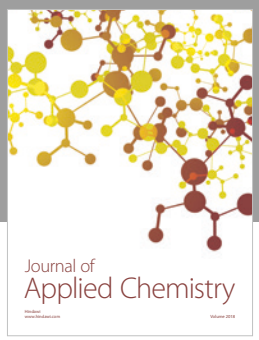

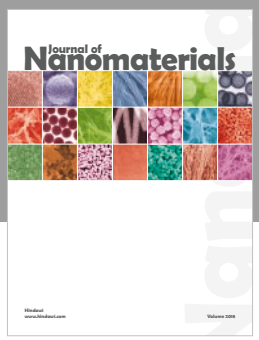

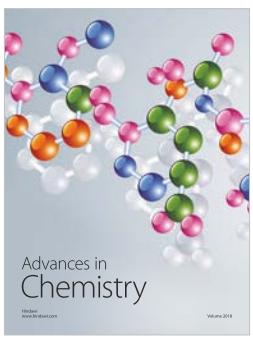

Hindawi

Submit your manuscripts at
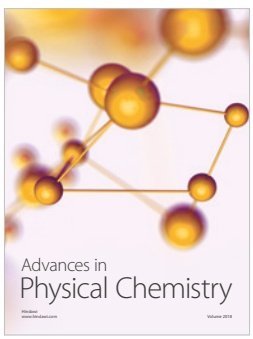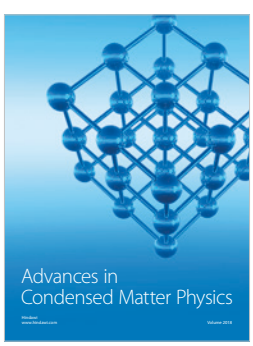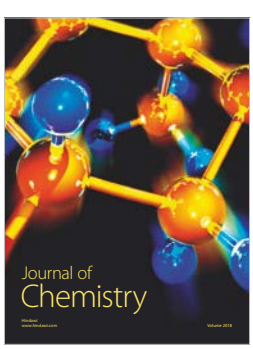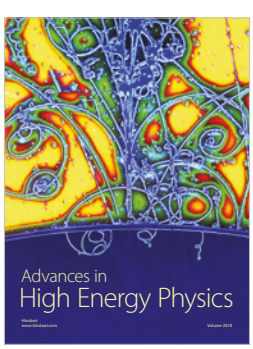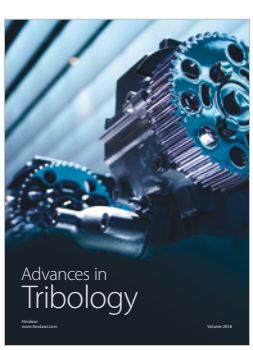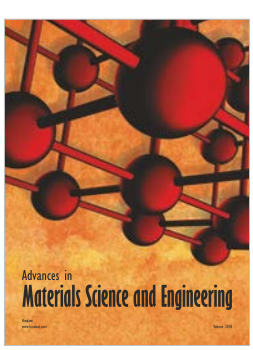
www.hindawi.com